IOP Publishing Nanotechnology
Nanotechnology 29 (2018) 014002 (9pp) https://doi.org/10.1088/1361-6528/aa9823

Heterojunctions of mixed phase TiO_2 nanotubes with Cu, CuPt, and Pt nanoparticles: interfacial band alignment and visible light photoelectrochemical activity

Piyush Kar[1,3,4], Yun Zhang[1,4], Najia Mahdi[1], Ujwal K Thakur[1], Benjamin D Wiltshire[1], Ryan Kisslinger[1] and Karthik Shankar[1,2,3]

[1] Department of Electrical and Computer Engineering, University of Alberta, 9211-116 St, Edmonton, AB, Canada T6G 1H9
[2] NRC National Institute for Nanotechnology, 11421 Saskatchewan Dr NW, Edmonton, AB, Canada T6G 2M9

E-mail: pkar1@ualberta.ca and kshankar@ualberta.ca

Received 4 September 2017, revised 17 October 2017
Accepted for publication 3 November 2017
Published 29 November 2017

Abstract

Anodically formed, vertically oriented, self-organized cylindrical TiO_2 nanotube arrays composed of the anatase phase undergo an interesting morphological and phase transition upon flame annealing to square-shaped nanotubes composed of both anatase and rutile phases. This is the first report on heterojunctions consisting of metal nanoparticles (NPs) deposited on square-shaped TiO_2 nanotube arrays (STNAs) with mixed rutile and anatase phase content. A simple photochemical deposition process was used to form Cu, CuPt, and Pt NPs on the STNAs, and an enhancement in the visible light photoelectrochemical water splitting performance for the NP-decorated STNAs was observed over the bare STNAs. Under narrow band illumination by visible photons at 410 nm and 505 nm, Cu NP-decorated STNAs performed the best, producing photocurrents 80% higher and 50 times higher than bare STNAs, respectively. Probing the energy level structure at the NP–STNA interface using ultraviolet photoelectron spectroscopy revealed Schottky barrier formation in the NP-decorated STNAs, which assists in separating the photogenerated charge carriers, as also confirmed by longer charge carrier lifetimes in NP-decorated STNAs. While all the NP-decorated STNAs showed enhanced visible light absorption compared to the bare STNAs, only the Cu NPs exhibited a clear plasmonic behavior with an extinction cross section that peaked at 550 nm.

Supplementary material for this article is available online

Keywords: built-in electric field, depletion, oxidative photoelectrochemistry, plasmonic photocatalysis, charge transfer, hybrid functional nanomaterials

(Some figures may appear in colour only in the online journal)

1. Introduction

Photoelectrochemical water splitting produces hydrogen, which assumes significance as a renewable energy source

[3] Author to whom any correspondence should be addressed.
[4] These authors contributed equally.

because of its usability as a clean fuel. Moreover, efficient photoelectrolysis modules can be integrated with excess electricity generating units, such as combustion turbines and solar panels, in order to store a portion of the generated electrical energy in the form of chemical energy, close to the point of generation. The key to efficient photoelectrocatalysis is the use of functionalized semiconductor nanostructures to overcome limitations inherent to band-structure and light absorption characteristics [1–5]. Vertically oriented TiO_2 nanotube arrays formed by electrochemical anodization constitute a scalable nanoarchitecture synthesized by solution processing, which at the same time possess a large surface area for heterogeneous catalysis and permits the orthogonalization of the competing processes of light absorption and charge separation [6–10]. In the case of TiO_2 nanotubes, several schemes can be found in the scientific literature to improve the light absorption characteristics, which include the use of pure rutile TiO_2 nanotubes (which have a slightly lower bandgap than anatase nanotubes) [11], cationic and anionic doping of TiO_2 nanotubes [12–16], defect engineering [17–21], incorporation of Mie scattering and photonic crystal effects for light trapping [22–27], and functionalization of the TiO_2 nanostructures with metal nanoparticles (NPs) and/or quantum dots (QDs) [1–4, 28–30].

Nanocomposites based on heterojunctions between TiO_2 nanotubes and metallic as well as bimetallic NPs have exhibited significant enhancements in photocatalytic activities [1], and therefore are a key driver of photocatalysis research using semiconductor nanomaterials. For instance, bimetallic CuPt coating on TiO_2 nanotubes with periodically modulated diameters exhibited a large increase in photocatalytic activity as well as specificity of product yield [4]. An understanding of the interfacial electric field and band bending present at such nanostructured metal–semiconductor interfaces is critical to the design of efficient photocatalysts. X-ray photoelectron spectroscopy (XPS) and ultraviolet photoelectron spectroscopy (UPS) enable the quantification of near surface valence band edges, which in turn enables determination of the interfacial band bending. We recently reported on interfacial electric field phenomena for metallic and bimetallic NPs incorporated on anatase TiO_2 nanotubes [1, 3].

TiO_2 nanotubes with rectangular or square-shaped cross-sections are a relatively unexplored nanomaterial on which we reported the first detailed studies in 2015 [11]. These nanotubes were found to consist of a mixture of anatase and rutile, and outperformed conventional anatase phase nanotubes for photoelectrochemical water splitting [11]. There is no data currently available on metal–semiconductor heterojunctions based on square-shaped TiO_2 nanotubes, thus motivating the current study. A second motivation was to obtain insights into the photoresponse of such heterojunctions under visible light illumination.

Ongoing research efforts are being directed at the development of materials that can harvest broad spectrum sunlight, support fast charge transfer to effect the oxygen evolution reaction and exhibit chemical stability over a wide range of pH [31]. From the standpoint of synthesis, it is desirable to obtain high quality catalysts, while emphasizing process scalability and cost [32]. Solution processing-based methodologies that are low cost and scalable, and can yield superior quality nanocomposites comprising of TiO_2 nanotubes with metal NPs and/or QDs, are a viable solution. To that end, using photodeposition, i.e. a simple solution processing method, we introduce Cu, Pt, and CuPt NPs decorated on the top surface and sidewalls of square-shaped TiO_2 nanotube arrays (STNAs). While the motivation for using Pt NPs is due its established catalytic effect, we used Cu NPs for their plasmonic behavior and CuPt NPs because of its emergence as a high performance photocatalyst for CO_2 reduction [3, 4]. Herein, we report the preparation, properties, and visible light photoelectrochemical splitting performance of the Cu-STNAs, Pt-STNAs, CuPt-STNAs and bare STNAs.

2. Experimental materials and methods

2.1. Synthesis of metal NP-decorated square-shaped TiO_2 nanotube arrays

TiO_2 nanotubes were prepared by anodization of Ti foil in ethylene glycol-based electrolyte at room temperature, and in a two-electrode electrochemical cell at a voltage of 30 V, with a graphite cathode. The recipe for anodization was comprised of 0.3 wt % NH4F (>98% purity, Fisher Chemical) and 4% deionized water (DI) in ethylene glycol (>99% purity, Fisher Chemical). The as-anodized nanotube arrays were annealed in air at 450 °C for 30 min, which was followed by flame annealing for 1 min using a propane torch. Deposition of Cu, CuPt, and Pt NPs involved a photochemical procedure, which is identical to the procedure reported elsewhere [3]. Briefly, the solutions for photodeposition of Cu, CuPt, and Pt NPs contained 2 mM of metal (Cu and/or Pt as applicable) acetylacetonate in methanol. The CuPt NP deposition solution contained 2 ml of copper acetylacetonate, 1 ml of platinum acetylacetonate and 1 ml of methanol. The Cu NP deposition solution contained 2 ml of copper acetylacetonate and 2 ml of methanol. The Pt NP deposition solution contained 1 ml of platinum acetylacetonate and 3 ml of methanol. Platinum acetylacetonate was of 98% purity and purchased from Strem Chemicals Inc. Copper acetylacetonate was of 99.8% purity and purchased from Fisher Chemical. The NP deposition process was carried out in a teflon cell of dimensions that matched the TiO_2 nanotube samples (1 cm × 3 cm in size), wherein 4 ml of the NP deposition solutions were used. NP deposition was performed by soaking the STNAs in the NP deposition solutions under irradiation of simulated solar light, at an intensity of one sun, from a solar simulator equipped with a class A AM1.5 filter. Subsequent to NP deposition, the samples were dried by exposure to air. A step-by-step process flow, starting from cleaning the Ti foils to formation of NPs deposited on STNAs, is shown in figure 1.

2.2. Characterization

Morphological imaging was by means of a field emission scanning electron microscope (FESEM, Hitachi-NB5000).

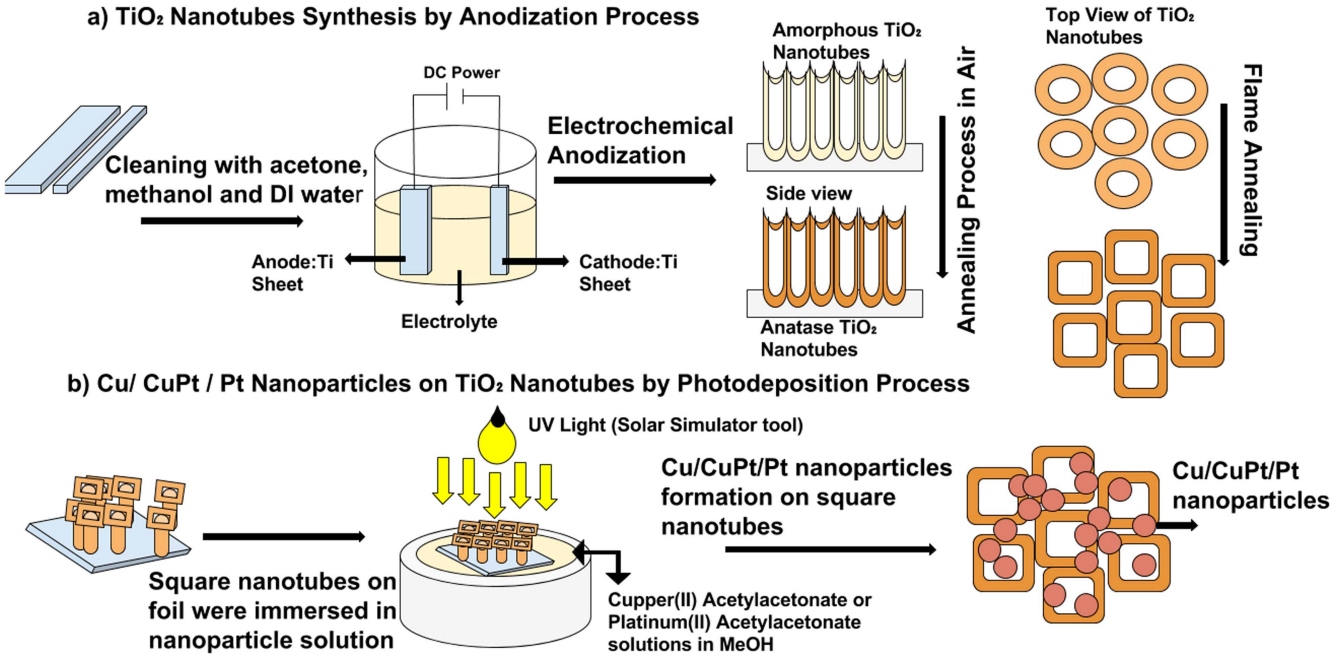

Figure 1. Process flow for (a) formation of square-shaped TiO_2 nanotube arrays (STNAs), and (b) deposition of Cu, CuPt, and Pt nanoparticles (NPs) on STNAs.

Crystalline phase characterization was accomplished by glancing angle x-ray diffraction (XRD) using a Bruker D8 Discover instrument with a sealed Cu Kα x-ray source. Raman spectra were collected with a Nicolet Almega XR Raman Spectrometer by using an incident laser wavelength of 532 nm and an incident power of 24 mW cm^{-2}. Optical spectra were collected using a Perkin Elmer Lambda-1050 UV–vis-NIR spectrophotometer equipped with an integrating sphere accessory. Steady state photoluminescence (PL) measurements were performed using a Varian Cary Eclipse fluorimeter. Composition and oxidation states characterization of the Cu, Pt, Ti, and O were performed by XPS using an Al Kα source at 1486.6 eV (Axis-Ultra, Kratos Analytical) under ultrahigh vacuum ($\sim 10^{-8}$ Torr). Data related to the *WF* and valence band maxima of the NP-decorated STNAs were obtained through UPS performed with a 21.21 eV He lamp source. Fluorescence lifetime imaging microscopy (FLIM) was performed by exciting the samples using 750 nm output of a femtosecond Ti:sapphire laser, and then imaging the resulting PL using a Zeiss LSM 510 NLO multi-photon microscope equipped with a FLIM module that consists of a Hamamatsu RS-39 multichannel plate detector, a filter wheel, and a Becker Hickl Q5 SPC730 photon-counting board.

2.3. Photoelectrochemical measurements

Light emitting diodes (LEDs) of desired wavelengths were used as visible light sources for photoelectrochemical measurements. The distance between the LED and the working electrode (i.e. the NP-decorated STNAs) was maintained at 2 cm. A schematic of the experimental set-up is as shown in figure S4, which is available online at stacks.iop.org/NANO/29/014002/mmedia in the supporting information. In the three-electrode system, we used a saturated KCl Ag/AgCl reference electrode, a graphite counter electrode, and a 1 M aqueous KOH electrolyte. Parafilm sealing was applied to all parts of the samples except for a 1 cm^2 window that was then exposed to the incident LED light. The input LED intensity was 24.94 mW cm^{-2} at 410 nm, and 10.98 mW cm^{-2} at 505 nm.

3. Results and discussion

The decoration of metal NPs is clearly seen in the FESEM images shown in figures 2(a), (b), and (c). The square-shaped pores of the STNAs are also evident from the FESEM images due to flame annealing by following a procedure reported earlier [11]. The average wall thickness of the nanotubes is $\sim$30 nm (figure 2(d), inset) and the length is $\sim 3\,\mu$m (from figure S1 in the supporting information). XRD patterns (figure 3) show the mixed anatase and rutile phase composition of the STNAs. Controlling and estimating the percentages of anatase and rutile phases is not within the scope of this report, and can be the subject of follow up work. FCC Pt (111) in Pt-STNAs and CuPt-STNAs are evident from the peaks at a 2θ angle of 39° (PDF#00-004-0802). FCC Cu (111) peaks in Cu-STNAs and CuPt-STNAs are at a 2θ angle of 43.40° in addition to a FCC Cu (200) peak at a 2θ angle of 50.5° (PDF#00-004-0836). Raman spectra collected from the samples (figure S3 in the supporting information) confirmed the presence of both rutile and anatase phases. The Pt (111) peak at a 2θ angle of 40.17°, Cu (111) peak at a 2θ angle of 43.40°, and CuPt (220) peak at a 2θ angle of 70.50° were used to estimate the average size of NPs supported on STNAs, as shown in figure S2 (supporting information). Applying the

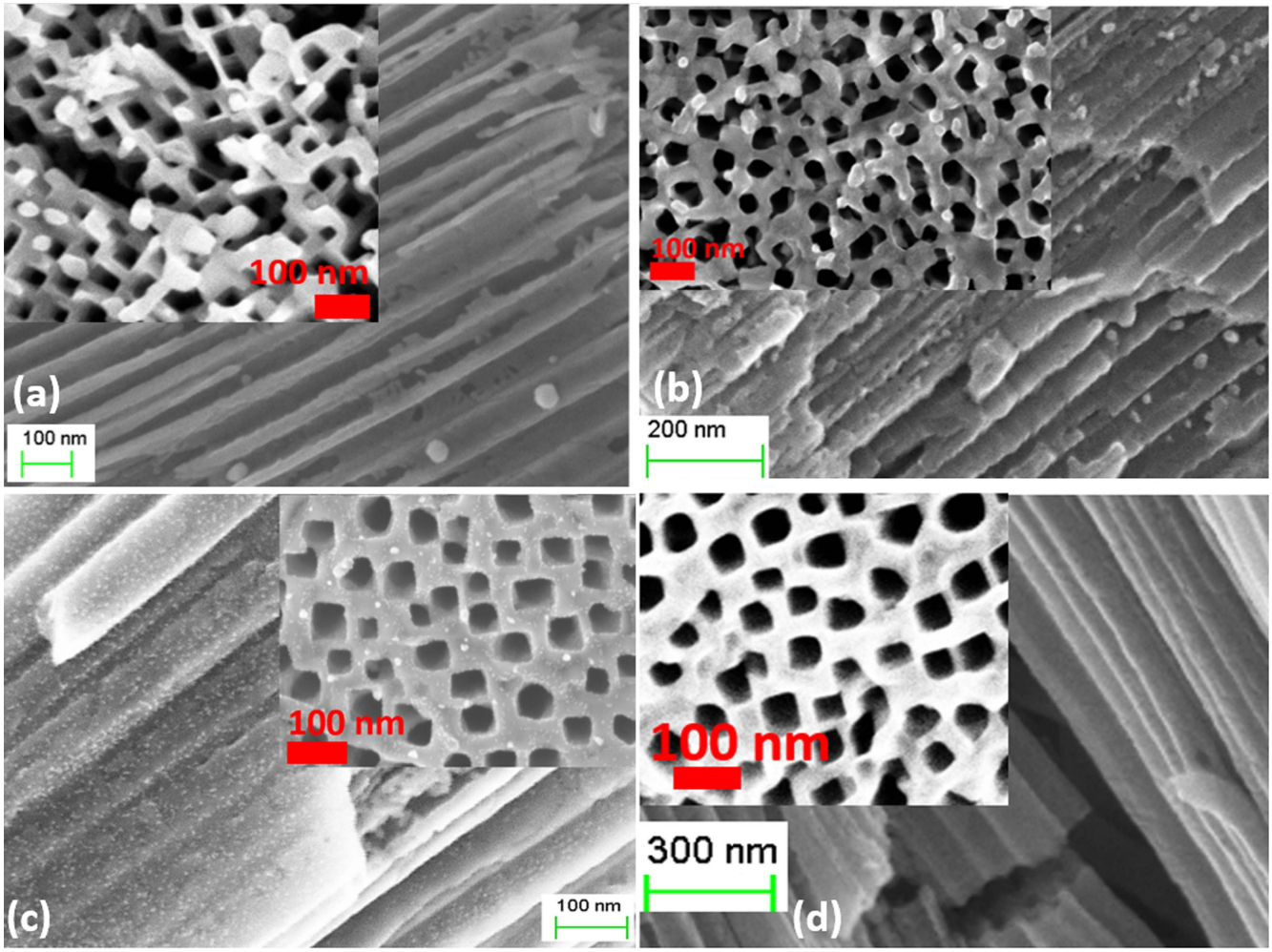

Figure 2. images of nanostructured heterojunctions (a) Cu-STNAs, (b) Pt-STNAs, (c) CuPt-STNAs, and (d) bare STNAs. Insets in each image show the top view.

Scherrer equation, the estimated sizes of the NPs are 66 nm, 33 nm, and 16 nm for Cu, Pt, and CuPt, respectively. It is, however, also evident from the FESEM images that that the size distribution of the NPs is wide, particularly for CuPt and Pt NPs. From the FESEM image (figure 2(a)) alone, it would appear that Cu NPs have a much larger size, and do not all make their way into the walls of the STNAs. However, the FESEM images need to be interpreted with caution since photodeposition can result in a bimodal size distribution consisting of a small number of larger-sized particles and a much larger number of extremely small particles (size <2 nm) that are not readily observable in scanning electron micrographs [3]. For NPs with a wide size distribution, the integral breadth method, which involves finding the ratio of the area under the relevant peak to the corresponding peak intensity, is a superior method to estimate the average crystallite size compared to the Scherrer equation method, wherein larger particles can contribute disproportionately to the observed peak width. Use of the Stokes–Wilson integral breadth

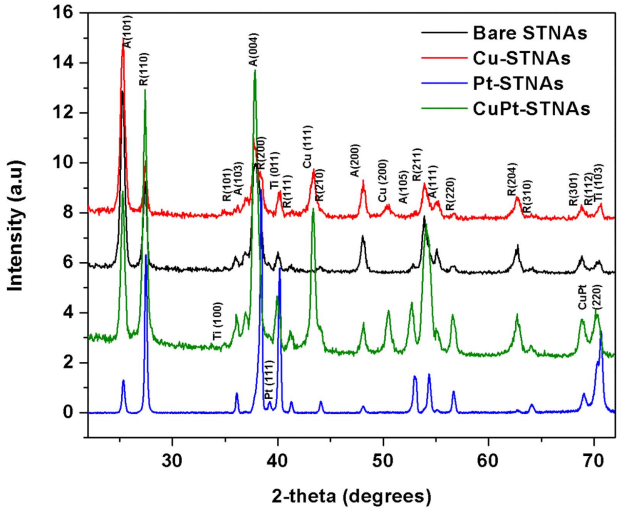

Figure 3. patterns of the Cu-STNAs, Pt-STNAs, CuPt-STNAs and bare STNAs. A denotes anatase and R denotes rutile.

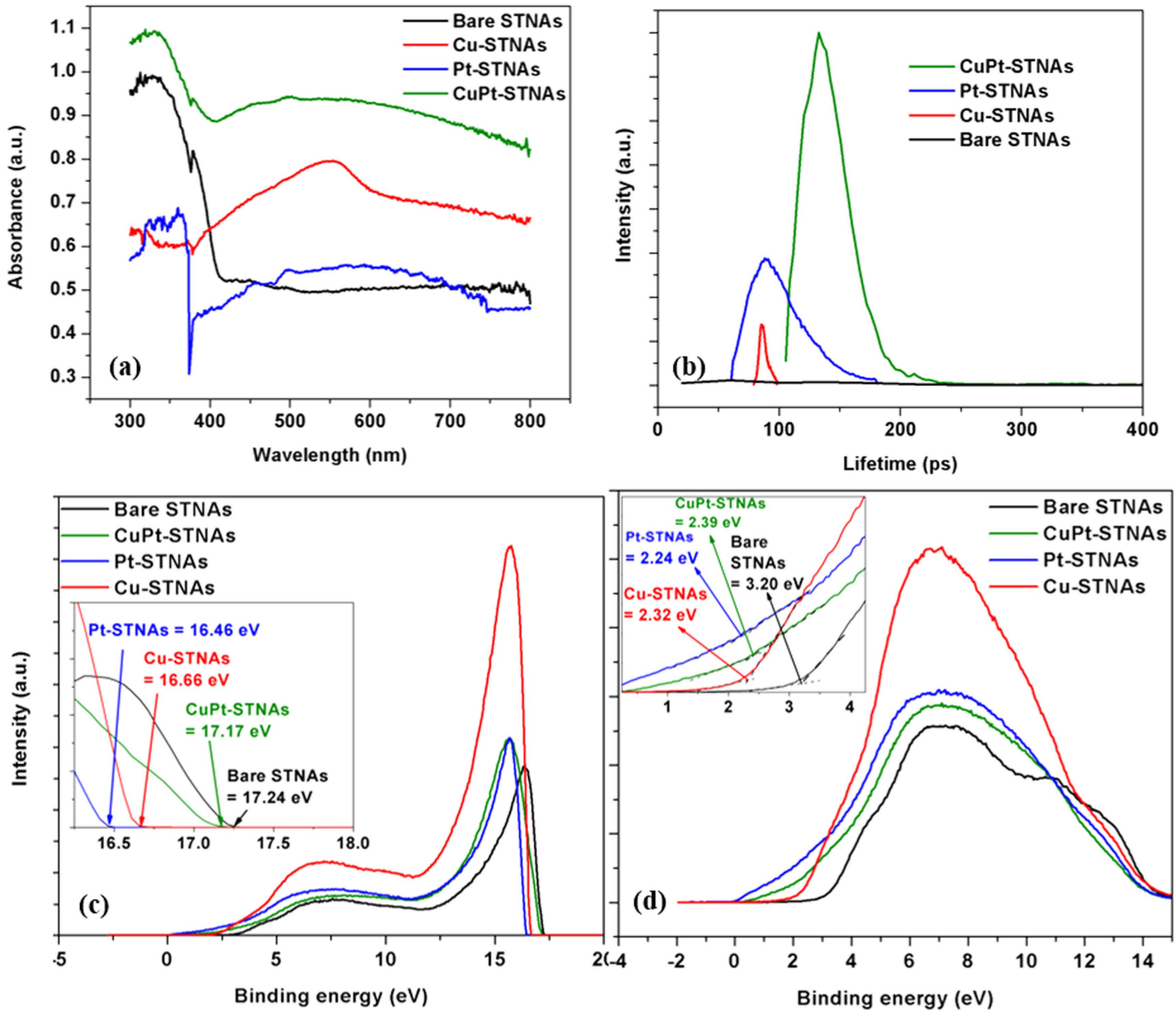

Figure 4. (a) UV–vis spectra, (b) fluorescence lifetime imaging microscopy plots, (c) ultraviolet photoelectron spectroscopy (UPS) secondary electron cut-off spectra, and (d) UPS valence band spectra of the Cu-STNAs, Pt-STNAs, CuPt-STNAs and bare STNAs.

method [33, 34] resulted in crystallite sizes of 15 nm, 40 nm, and 40 nm for Cu, Pt, and CuPt NPs, respectively.

UV–vis spectra (figure 4(a)) of the NP-decorated STNAs show broad absorption bands centered at ∼600 nm that extend beyond 700 nm for the CuPt-STNAs and Pt-STNAs. Cu-STNAs, on the other hand exhibit a localized surface plasmon resonance centered at ∼550 nm. The broad peaks are consistent with a large size distribution of the NPs. Cu-STNAs and Pt-STNAs exhibit an anomalous decrease in the UV absorption for photons larger than the bandgap of TiO_2, where a strong absorption by TiO_2 is expected (and observed for STNAs and CuPt-STNAs). Because the Ti substrates are non-transparent, the UV–vis spectra displayed in figure 4(a) were obtained through measurements of the diffuse reflectance of the samples wherein scattered photons are collected by the integrating sphere. The data in figure 4(a) strongly indicates that scattering of UV photons by Cu NPs and Pt NPs dominates over TiO_2 absorption. As probed using FLIM (figure 4(b)), the charge carrier lifetimes in the NP-decorated STNAs are 100 ps, 170 ps, and 250 ps for Cu-STNAs, Pt-STNAs, and CuPt-STNAs, respectively. The charge carrier lifetime in bare STNAs is shorter than in NP-decorated STNAs, and was not detectable because of the very low emission intensity coupled with short lifetime. The steady state PL spectra of all samples studied in this report are rather similar as seen in figure S5 in the supporting information, thus indicating the absence of any new emission pathways due to decoration of the STNAs by metal NPs. Therefore, changes in the PL lifetime are primarily attributable to improved charge separation due to built-in electric fields arising from the metal NP-STNA nanotube heterojunctions.

Work function (*WF*) values were determined from the UPS work function spectra, shown in figure 4(c) (details in the inset), by using the equation $WF = 21.21 - E_{\text{cut-off}}$,

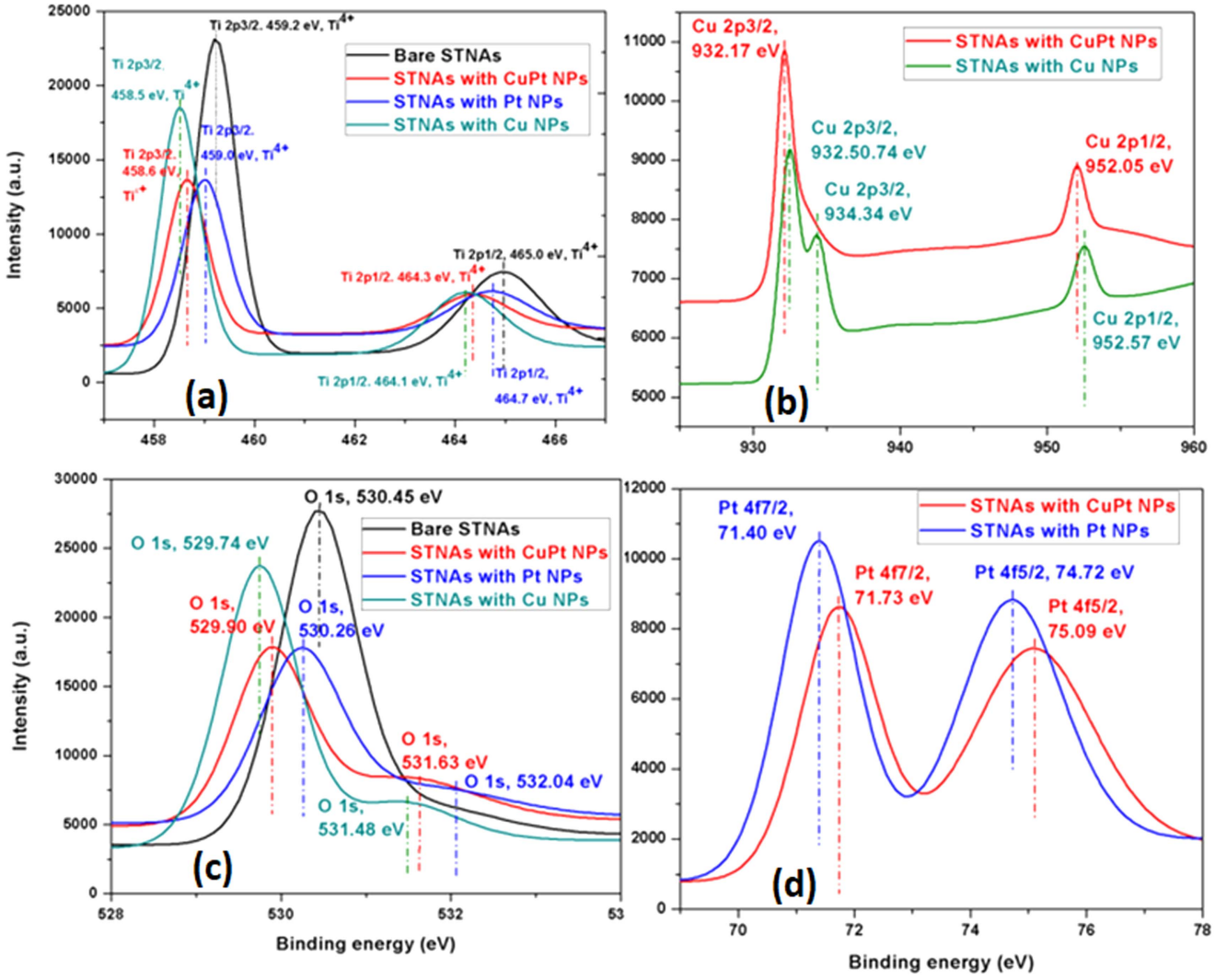

Figure 5. (a) Ti 2p, (b) Cu 2p, (c) O 1s, and (d) Pt 4f XPS spectra of Cu-STNAs, Pt-STNAs, CuPt-STNAs and bare STNAs.

where 21.21 eV is the energy of the incident He laser, and $E_{\text{cut-off}}$ is the cut-off energy. *WF* values for the Cu-STNAs, CuPt-STNAs, and Pt-STNAs are 4.55 eV, 4.04 eV, and 4.75 eV, respectively, and the same for the bare STNAs is 3.97 eV. The positions of the valence band maxima (VB_{max}) with respect to the vacuum level, estimated from the UPS valence band spectra (figure 4(d)), for Cu-STNAs, CuPt-STNAs and Pt-STNAs are 2.32 eV, 2.39 eV, and 2.24 eV, respectively (details in the inset of figure 4(d)). The VB_{max} for the bare STNAs, also estimated from figure 4(d), is 3.20 eV. Using the values of VB_{max} and *WF*, band diagrams of the NP-decorated STNAs were drawn, and are shown in figure 6(a). Upward band bending for all three NP-decorated STNAs is visualized on the basis on the VB_{max} and *WF* data, and imply Schottky barrier formation (as shown in figure 6(a)). NPs with sizes >2 nm, in which the metallic behavior is fully developed, exhibit a sharp cut-off at the Fermi level ($E_b = 0$ in figure 4(d)) [3]. In figures 4(c) and (d), it is seen that CuPt-STNAs and Pt-STNAs have a cut-off close to the Fermi level; however, this cut-off is not sharp. For Cu-STNAs, the cut-off does not occur close to the Fermi level. Taken together, these results suggest that there exists a subset of sub-2 nm sized NPs in each of the samples studied.

XPS (figure 5) enabled detection of the presence of metal NPs, and revealed information pertinent to the composition of the NP–STNA hybrids. The presence of Cu in CuPt-STNAs is confirmed by the Cu $2p_{3/2}$ peak at 932.17 eV and Cu $2p_{1/2}$ peak at 952.05 eV [35, 36] in figure 5(b); and the presence of Pt in CuPt-STNAs is confirmed by the Pt $4f_{7/2}$ peak at 71.73 eV and Pt $4f_{5/2}$ peak at 75.09 eV in figure 5(d) [37]. A small shift in the binding energy of Pt 4 f in CuPt-STNAs is observed as well, which may be attributed to size effects and the interaction of Cu and Pt in the CuPt NPs on the TiO_2 support [38–40]. In the Cu NPs in Cu-STNAs, the presence of elemental Cu is confirmed by the Cu $2p_{3/2}$ at 932.17 eV, while the peak Cu $2p_{3/2}$ at 934.34 eV is likely due to oxidation of Cu [35]. It must however be noted that the peak for oxidized Cu is considerably smaller than for elemental Cu in Cu-STNAs. Moreover, the Cu $2p_{1/2}$ peak at 952.57 eV supports the presence of elemental Cu. In the Pt NPs in Pt-STNAs, the Pt $4f_{7/2}$ peak at 71.40 eV and the Pt $4f_{5/2}$ peak at 74.72 eV can be attributed to metallic Pt [3, 37]. Metallic Cu (in Cu-STNAs)

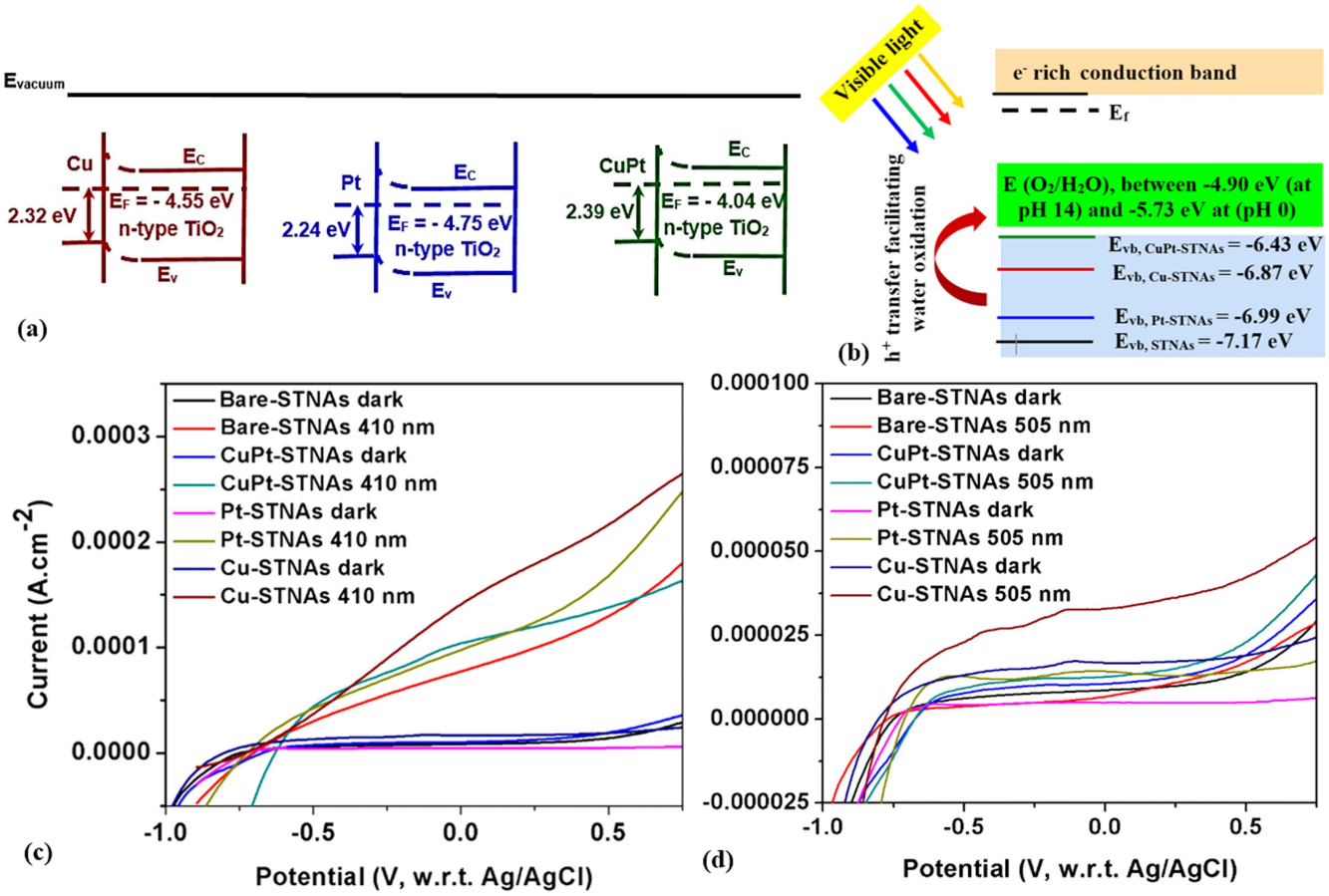

Figure 6. (a) Band diagrams of Cu-STNAs, Pt-STNAs, and CuPt-STNAs; (b) schematic of the water oxidation processes from thermodynamic standpoint; (c) and (d) linear sweep voltammograms, showing plots of photocurrent versus voltage under near-monochromatic visible light illumination using a 410 nm LED source and 505 nm LED source, respectively.

and Pt (in Pt-STNAs) NPs detected by XPS are consistent with findings from our XRD analysis. XPS spectra for Ti in Cu-STNAs and CuPt-STNAs (figure 5(a)) show a Ti $2p_{3/2}$ peak near 458.5 eV and Ti $2p_{1/2}$ peak near 464.2 eV, confirming stoichiometric TiO2 or Ti^{4+} states [3]. Small shifts of the Ti peak in Pt-STNAs and bare STNAs confirm Ti^{4+} as well, and are consistent with the processes of annealing followed by flame annealing, whereby most of the oxygen vacancy defects are annihilated [11]. XPS spectra of O 1 s (figure 5(c)) show a small peak shift in the Cu-STNAs and CuPt-STNAs toward lower binding energies, which is in agreement with our prior finding [3]. Furthermore, O 1 s peaks near 531 eV for Pt-STNAs and bare STNAs agree with our prior finding for rutile-containing TiO_2 nanotubes [11].

Figures 6(c) and (d) show linear sweep voltammograms of Cu-STNAs, Pt-STNAs, CuPt-STNAs, and bare STNAs, obtained by exposure to 410 nm and 505 nm illumination, respectively. Significantly higher photoelectrochemical performance, using a 410 nm LED (figure 6(c)), was exhibited by all three NP-decorated STNAs compared to the bare STNAs. Under 410 nm illumination, the Pt-STNAs and CuPt-STNAs produced 20% higher photocurrents compared to bare STNAs while the Cu-STNAs produced an 80% increase in the photocurrent. The oxygen evolution reaction proceeds first by electron–hole separation via light absorption followed by donation of photogenerated holes with high oxidizing power to hydroxyl ions in the electrolyte. Figure 6(b) shows favorable energetics for a water oxidation reaction by hole-injection at the valence band edge of the NP-decorated STNAs and bare STNAs. Meanwhile, the relative higher photoelectrocatalytic activity of the NP-decorated STNAs than the bare STNAs indicate chemically stable NPs in alkaline conditions at pH 14; their more negative flat-band potential values obtained from Mott–Schottky plots (figure S6 in the supporting information) compared to the bare STNAs indicate their relatively faster response to applied potential, and hence better suitability as photoelectrocatalysts. The upward band bending due to Schottky barrier formation in the NP-decorated STNAs coupled with longer charge carrier lifetimes (as evident from FLIM data) produces improved charge separation (electrons directed through the Ti substrate to the counter electrode, and holes directed toward the electrolyte), which in turn is responsible for the superior performance of the NP-decorated STNAs. For 505 nm illumination, Cu-STNAs significantly outperform the other photoanodes in the generation of photocurrents, as seen in figure 6(d), producing a nearly 50-fold increase in the photocurrent compared to bare STNAs. We surmise that the more efficient sensitization of the Cu-STNAs for photoelectrochemical water splitting stimulated by 505 nm illumination is likely due to

hot electron injection over the Schottky barrier mediated by the plasmon resonance effect observed in figure 4(a).

Tafel slopes (figure S7 in the supporting information), as determined from the 410 nm illuminated linear sweep voltammograms (figure 6(c)), are 0.277, 0.317, 0.428, and 0.310 V decade^{-1} for Cu-STNAs, Pt-STNAs, CuPt-STNAs, and bare STNAs, respectively. These Tafel slopes values are high because of the rectifying effect of the NP-decorated STNAs and the long length (2 μm) of the TiO_2 nanotubes that impede electron transport to the Ti support (see figures S1 and S4 in the supporting information). The Tafel slopes, however, imply the lowest electric field bias dependent performance for the Cu-SNTAs followed by bare STNAs, CuPt-STNAs, and Pt-STNAs.

4. Conclusion

Chemically stable Cu, Pt, and CuPt NP-decorated TiO_2 nanotube arrays with square cross-sections having mixed anatase and rutile phases were prepared using facile solution processing, and were found to exhibit better visible light photoelectrochemical water splitting performance than bare nanotubes. The interfacial electric field characterization by UPS confirmed formation of a Schottky barrier for the NP-decorated STNAs. While the Pt-STNAs and CuPt-STNAs absorb light over a broad spectrum ranging from the violet to the near-infrared, the Cu-STNAs exhibit a distinct plasmon resonance. The vastly superior performance of the Cu NP-decorated TiO_2 nanotubes is attributed to a combination of a plasmonic photocatalytic effect and improved charge separation.

Acknowledgments

All authors thank the Natural Sciences and Engineering Research Council (NSERC), the National Research Council (NRC), and CMC Microsystems for direct and indirect (equipment use) financial support. B D W and U K T were supported by graduate student scholarships from Alberta Innovates. Some device fabrication and testing used research infrastructure made possible by a Leaders Opportunity Fund grant to K S from the Canada Foundation for Innovation and the Alberta Small Equipment Grants Program. We acknowledge use of the following facilities: the National Research Council - National Institute for Nanotechnology (NRC-NINT) Electron Microscopy Lab, the Cell Imaging Facility, and the University of Alberta Nanofab.

ORCID iDs

Karthik Shankar https://orcid.org/0000-0001-7347-3333

References

[1] Kar P, Farsinezhad S, Mahdi N, Zhang Y, Obuekwe U, Sharma H, Shen J, Semagina N and Shankar K 2016 Enhanced CH_4 yield by photocatalytic CO_2 reduction using TiO_2 nanotube arrays grafted with Au, Ru, and ZnPd nanoparticles *Nano Res.* **9** 3478–93

[2] Kwon S, Lee S J, Kim S M, Lee Y, Song H and Park J Y 2015 Probing the nanoscale Schottky barrier of metal/semiconductor interfaces of Pt/CdSe/Pt nanodumbbells by conductive-probe atomic force microscopy *Nanoscale* **7** 12297–301

[3] Farsinezhad S, Sharma H and Shankar K 2015 Interfacial band alignment for photocatalytic charge separation in TiO_2 nanotube arrays coated with CuPt nanoparticles *Phys. Chem. Chem. Phys.* **17** 29723–33

[4] Zhang X, Han F, Shi B, Farsinezhad S, Dechaine G P and Shankar K 2012 Photocatalytic conversion of diluted CO_2 into light hydrocarbons using periodically modulated multiwalled nanotube arrays *Angew. Chem., Int. Ed.* **51** 12732–5

[5] Zhou X, Liu N and Schmuki P 2017 Photocatalysis with TiO_2 nanotubes: 'colorful' reactivity and designing site-specific photocatalytic centers into TiO_2 nanotubes *ACS Catal.* **7** 3210–35

[6] Shankar K, Basham J I, Allam N K, Varghese O K, Mor G K, Feng X, Paulose M, Seabold J A, Choi K-S and Grimes C A 2009 Recent advances in the use of TiO_2 nanotube and nanowire arrays for oxidative photoelectrochemistry *J. Phys. Chem.* C **113** 6327–59

[7] Mohammadpour A, Kar P, Wiltshire B D, Askar A M and Shankar K 2015 Electron transport, trapping and recombination in anodic TiO_2 nanotube arrays *Curr. Nanosci.* **11** 593–614

[8] Reyes-Gil K R and Robinson D B 2013 WO_3-enhanced TiO_2 nanotube photoanodes for solar water splitting with simultaneous wastewater treatment *ACS Appl. Mater. Interfaces* **5** 12400–10

[9] Xiao F-X, Miao J, Tao H B, Hung S-F, Wang H-Y, Yang H B, Chen J, Chen R and Liu B 2015 One-dimensional hybrid nanostructures for heterogeneous photocatalysis and photoelectrocatalysis *Small* **11** 2115–31

[10] Rambabu Y, Jaiswal M and Roy S C 2016 Enhanced photoelectrochemical performance of reduced graphene-oxide wrapped TiO_2 multi-leg nanotubes *J. Electrochem. Soc.* **163** H652–6

[11] Kar P, Zhang Y, Farsinezhad S, Mohammadpour A, Wiltshire B D, Sharma H and Shankar K 2015 Rutile phase n-and p-type anodic titania nanotube arrays with square-shaped pore morphologies *Chem. Commun.* **51** 7816–9

[12] Shankar K, Paulose M, Mor G K, Varghese O K and Grimes C A 2005 A study on the spectral photoresponse and photoelectrochemical properties of flame-annealed titania nanotube-arrays *J. Phys. D: Appl. Phys.* **38** 3543–9

[13] Shankar K, Tep K C, Mor G K and Grimes C A 2006 An electrochemical strategy to incorporate nitrogen in nanostructured TiO_2 thin films: modification of bandgap and photoelectrochemical properties *J. Phys. D: Appl. Phys.* **39** 2361–6

[14] Xu B-L, Liu C-X, Sun H-Y and Zhong Y-R 2014 Fabrication and photocatalytic properties of pure and cation doped TiO_2 nanotube arrays *Optoelectron. Lett.* **10** 84–7

[15] Piskunov S, Lisovski O, Begens J, Bocharov D, Zhukovskii Y F, Wessel M and Spohr E 2015 C-, N-, S-, and Fe-doped TiO_2 and $SrTiO_3$ nanotubes for visible-light-driven photocatalytic water splitting: prediction from first principles *J. Phys. Chem.* C **119** 18686–96

[16] Zhu M, Zhai C, Qiu L, Lu C, Paton A S, Du Y and Goh M C 2015 New method to synthesize S-doped TiO_2 with stable and highly efficient photocatalytic performance under indoor sunlight irradiation *ACS Sustain. Chem. Eng.* **3** 3123–9

[17] Dong J, Han J, Liu Y, Nakajima A, Matsushita S, Wei S and Gao W 2014 Defective black TiO_2 synthesized via

anodization for visible-light photocatalysis *ACS Appl. Mater. Interfaces* **6** 1385–8
[18] Cui H, Zhao W, Yang C, Yin H, Lin T, Shan Y, Xie Y, Gu H and Huang F 2014 Black TiO_2 nanotube arrays for high-efficiency photoelectrochemical water-splitting *J. Mater. Chem.* A **2** 8612–6
[19] Liu N, Schneider C, Freitag D, Zolnhofer E M, Meyer K and Schmuki P 2016 Noble-metal-free photocatalytic H_2 generation: active and inactive 'black' TiO_2 nanotubes and synergistic effects *Chem. Eur. J.* **22** 13810–4
[20] Liu N, Schneider C, Freitag D, Hartmann M, Venkatesan U, Müller J, Spiecker E and Schmuki P 2014 Black TiO_2 nanotubes: cocatalyst-free open-circuit hydrogen generation *Nano Lett.* **14** 3309–13
[21] Liu N *et al* 2015 'Black' TiO_2 nanotubes formed by high-energy proton implantation show noble-metal-co-catalyst free photocatalytic H_2-evolution *Nano Lett.* **15** 6815–20
[22] Lin J, Liu K and Chen X 2011 Synthesis of periodically structured titania nanotube films and their potential for photonic applications *Small* **7** 1784–9
[23] Yip C T, Huang H, Zhou L, Xie K, Wang Y, Feng T, Li J and Tam W Y 2011 Direct and seamless coupling of TiO_2 nanotube photonic crystal to dye-sensitized solar cell: a single-step approach *Adv. Mater.* **23** 5624–8
[24] Amirsolaimani B, Zhang X, Han F, Farsinezhad S, Mohammadpour A, Dechaine G and Shankar K 2013 Effect of the nature of the metal Co-catalyst on CO_2 photoreduction using fast-grown periodically modulated titanium dioxide nanotube arrays (PMTiNTs) *MRS Symp. Proc.* **1578**
[25] Mohammadpour A, Farsinezhad S, Hsieh L-H and Shankar K 2013 Multipodal and multilayer TiO_2 nanotube arrays: hierarchical structures for energy harvesting and sensing *MRS Symp. Proc.* 1552, pp 29–34
[26] Zhang Z, Zhang L, Hedhili M N, Zhang H and Wang P 2013 Plasmonic gold nanocrystals coupled with photonic crystal seamlessly on TiO_2 nanotube photoelectrodes for efficient visible light photoelectrochemical water splitting *Nano Lett.* **13** 14–20
[27] Mohammadpour A and Shankar K 2010 Anodic TiO_2 nanotube arrays with optical wavelength-sized apertures *J. Mater. Chem.* **20** 8474–7
[28] Kang Q, Liu S, Yang L, Cai Q and Grimes C A 2011 Fabrication of PbS nanoparticle-sensitized TiO_2 nanotube arrays and their photoelectrochemical properties *ACS Appl. Mater. Interfaces* **3** 746–9
[29] Banerjee S, Mohapatra S K, Das P P and Misra M 2008 Synthesis of coupled semiconductor by filling 1D TiO_2 nanotubes with CdS *Chem. Mater.* **20** 6784–91
[30] Yang L, Luo S, Liu R, Cai Q, Xiao Y, Liu S, Su F and Wen L 2010 Fabrication of CdSe nanoparticles sensitized long TiO_2 nanotube arrays for photocatalytic degradation of anthracene-9-carbonxylic acid under green monochromatic light *J. Phys. Chem.* C **114** 4783–9
[31] Roger I, Shipman M A and Symes M D 2017 Earth-abundant catalysts for electrochemical and photoelectrochemical water splitting *Nat. Rev. Chem.* **1** 0003
[32] Rao B M and Roy S C 2014 Solvothermal processing of amorphous TiO_2 nanotube arrays: achieving crystallinity at a lower thermal budget *J. Phys. Chem.* C **118** 1198–205
[33] Stokes A and Wilson A 1942 *A Method of Calculating the Integral Breadths of Debye–Scherrer Lines* vol 38 (Cambridge: Cambridge University Press) pp 313–22
[34] Scardi P, Leoni M and Delhez R 2004 Line broadening analysis using integral breadth methods: a critical review *J. Appl. Crystallogr.* **37** 381–90
[35] Mansour A 1994 Copper Mg Kα XPS spectra from the physical electronics model 5400 spectrometer *Surf. Sci. Spectra* **3** 202–10
[36] Poulston S, Parlett P, Stone P and Bowker M 1996 Surface oxidation and reduction of CuO and Cu_2O studied using XPS and XAES *Surf. Interface Anal.* **24** 811–20
[37] Hüfner S and Wertheim G 1975 Core-line asymmetries in the x-ray-photoemission spectra of metals *Phys. Rev.* B **11** 678
[38] Eberhardt W, Fayet P, Cox D, Fu Z, Kaldor A, Sherwood R and Sondericker D 1990 Photoemission from mass-selected monodispersed Pt clusters *Phys. Rev. Lett.* **64** 780
[39] Liu Y, Huang Y, Xie Y, Yang Z, Huang H and Zhou Q 2012 Preparation of highly dispersed CuPt nanoparticles on ionic-liquid-assisted graphene sheets for direct methanol fuel cell *Chem. Eng. J.* **197** 80–7
[40] Schierbaum K, Fischer S, Torquemada M, De Segovia J, Roman E and Martin-Gago J 1996 The interaction of Pt with TiO_2 (110) surfaces: a comparative XPS, UPS, ISS, and ESD study *Surf. Sci.* **345** 261–73

Supporting Information

Heterojunctions of mixed phase TiO_2 nanotubes with Cu, CuPt and Pt nanoparticles: Interfacial band alignment and visible light photoelectrochemical activity

Piyush Kar[1*,#], Yun Zhang[1,#], Najia Mahdi[1], Ujwal Thakur[1], Benjamin D. Wiltshire[1], Ryan Kisslinger and Karthik Shankar[1,2,*]

[1]*Department of Electrical and Computer Engineering, University of Alberta, 9211 - 116 St, Edmonton, Alberta, Canada T6G 1H9*

[2]*NRC National Institute for Nanotechnology, 11421 Saskatchewan Dr NW, Edmonton, AB T6G 2M9*

*** Corresponding Authors:**

Karthik Shankar; email: kshankar@ualberta.ca

Piysuh Kar; email: pkar1@ualberta.ca

 # These authors contributed equally

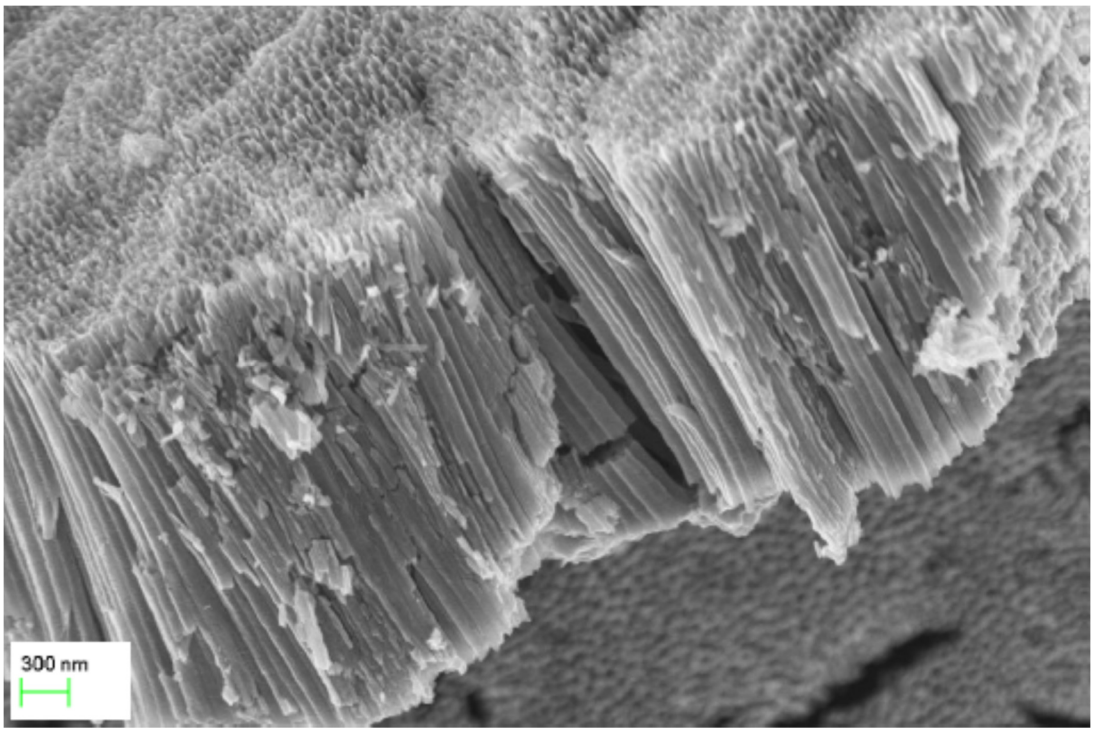

Fig. S1. Cross-section FESEM image of the bare STNAs showing the length of the nanotubes

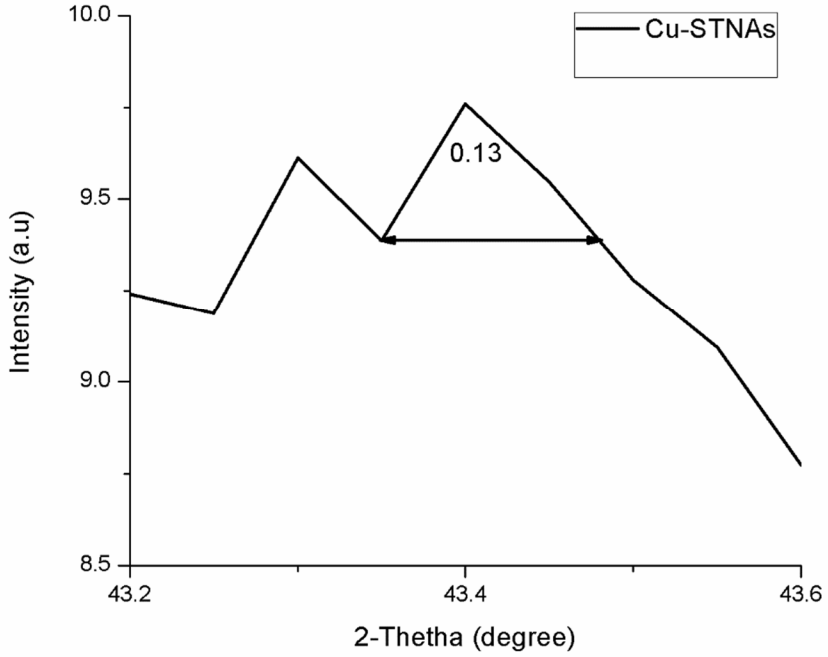
Cu-STNAs
0.13
10.0
9.5
9.0
8.5
Intensity (a.u)
43.2
43.4
43.6
2-Thetha (degree)

(a)

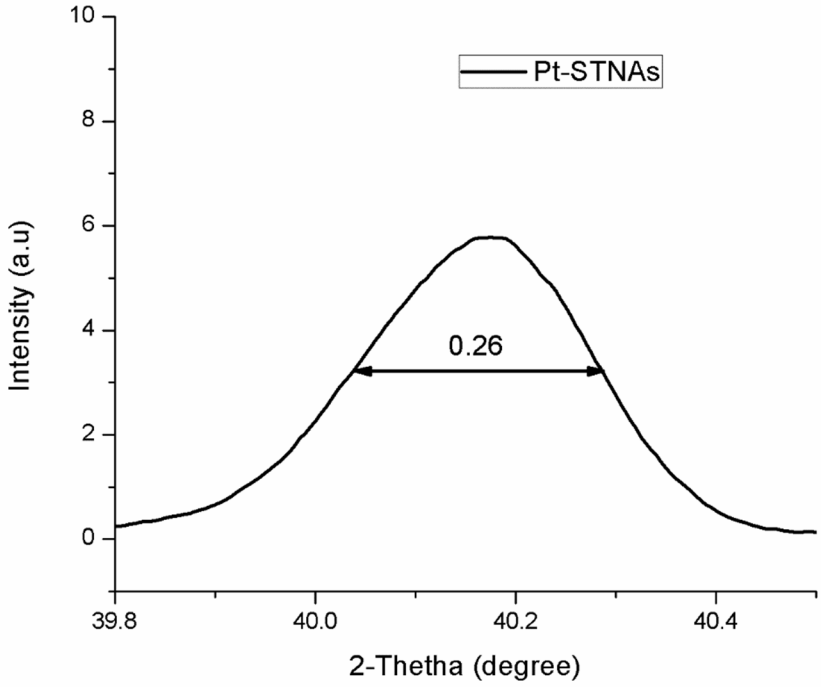
Pt-STNAs
Intensity (a.u)
2-Thetha (degree)
0.26
10
8
6
4
2
0
39.8
40.0
40.2
40.4

(b)

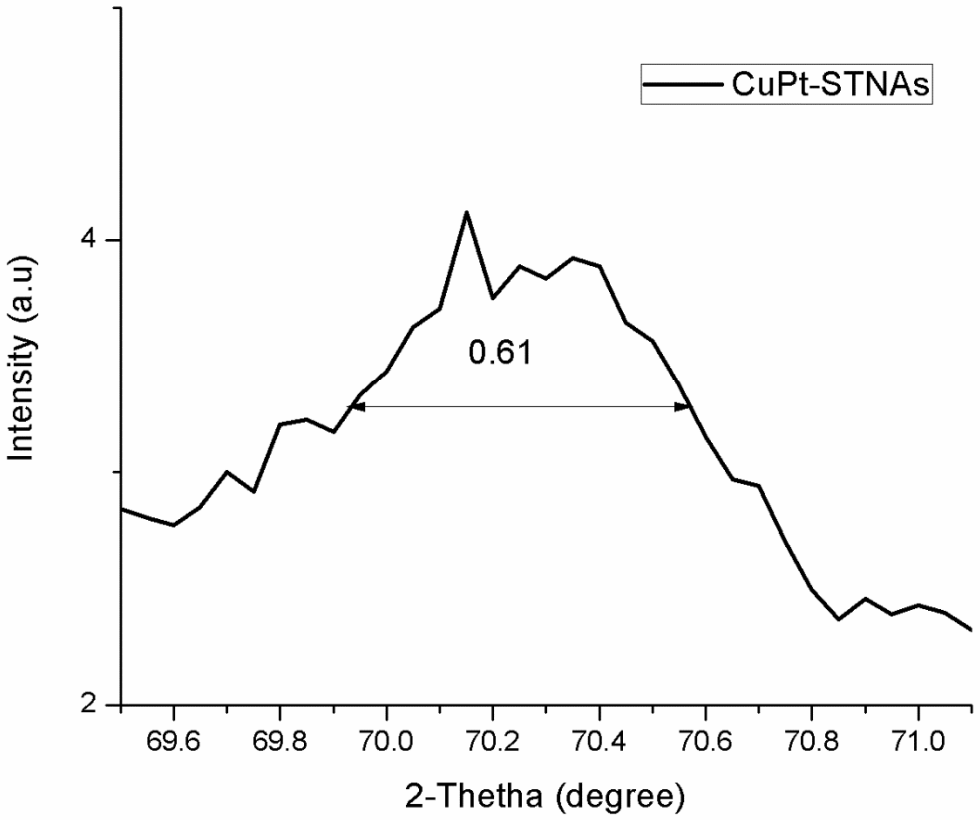

(c)

Fig. S2. (a), (b) and (c) are plots of peaks of Cu (111), Pt (111) and CuPt (002), respectively. The peak widths at half maximum, as indicated in the plots were used to determine the sizes of the metal nanoparticles.

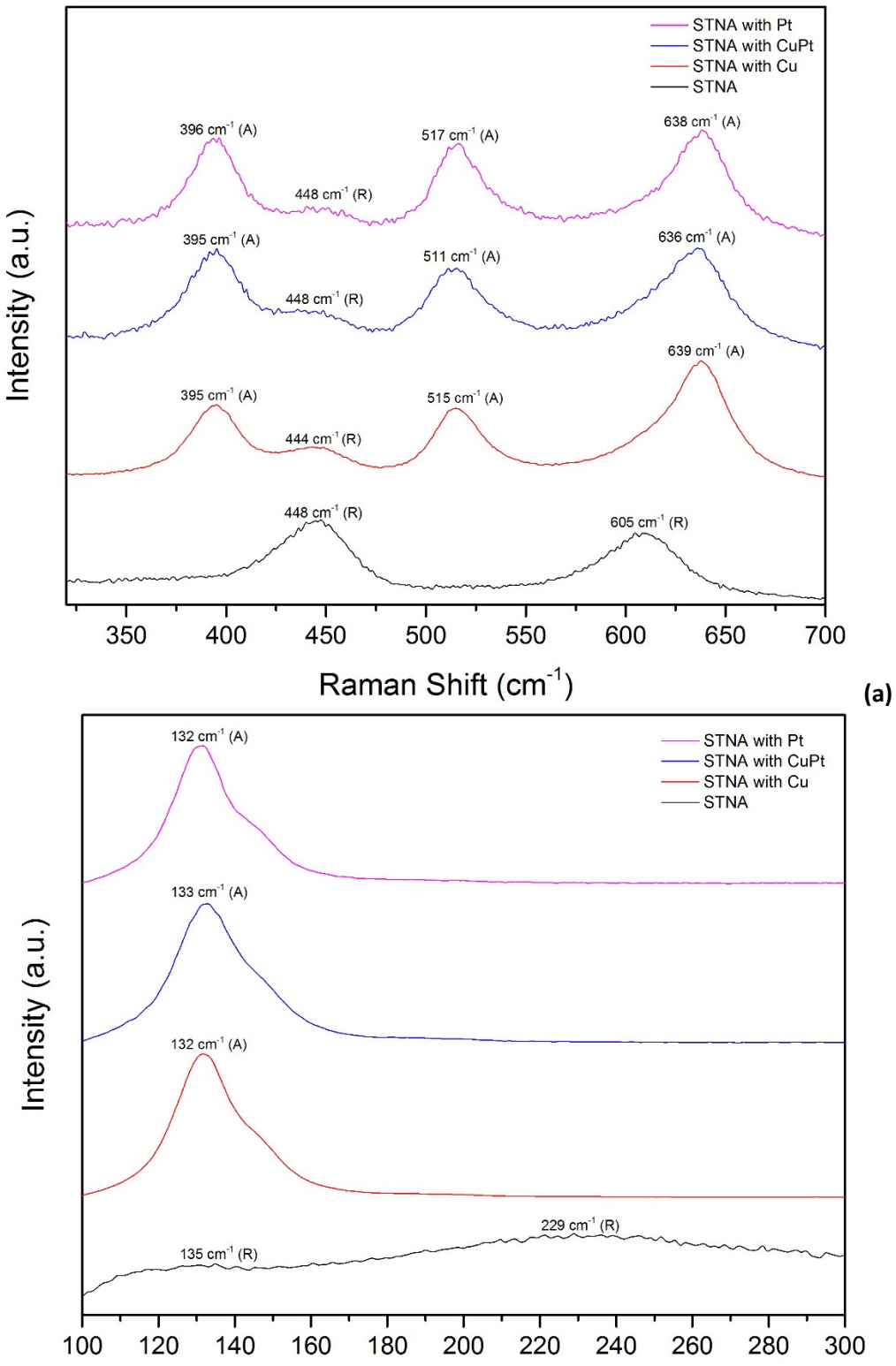

Fig. S3. (a) and (b) are Raman spectra of the NP incorporated STNAs showing anatase and rutile peaks, which agree well with our previous report.[1] NPs being metallic do not exhibit Raman peaks. In the figures, A denotes anatase and R denotes rutile.

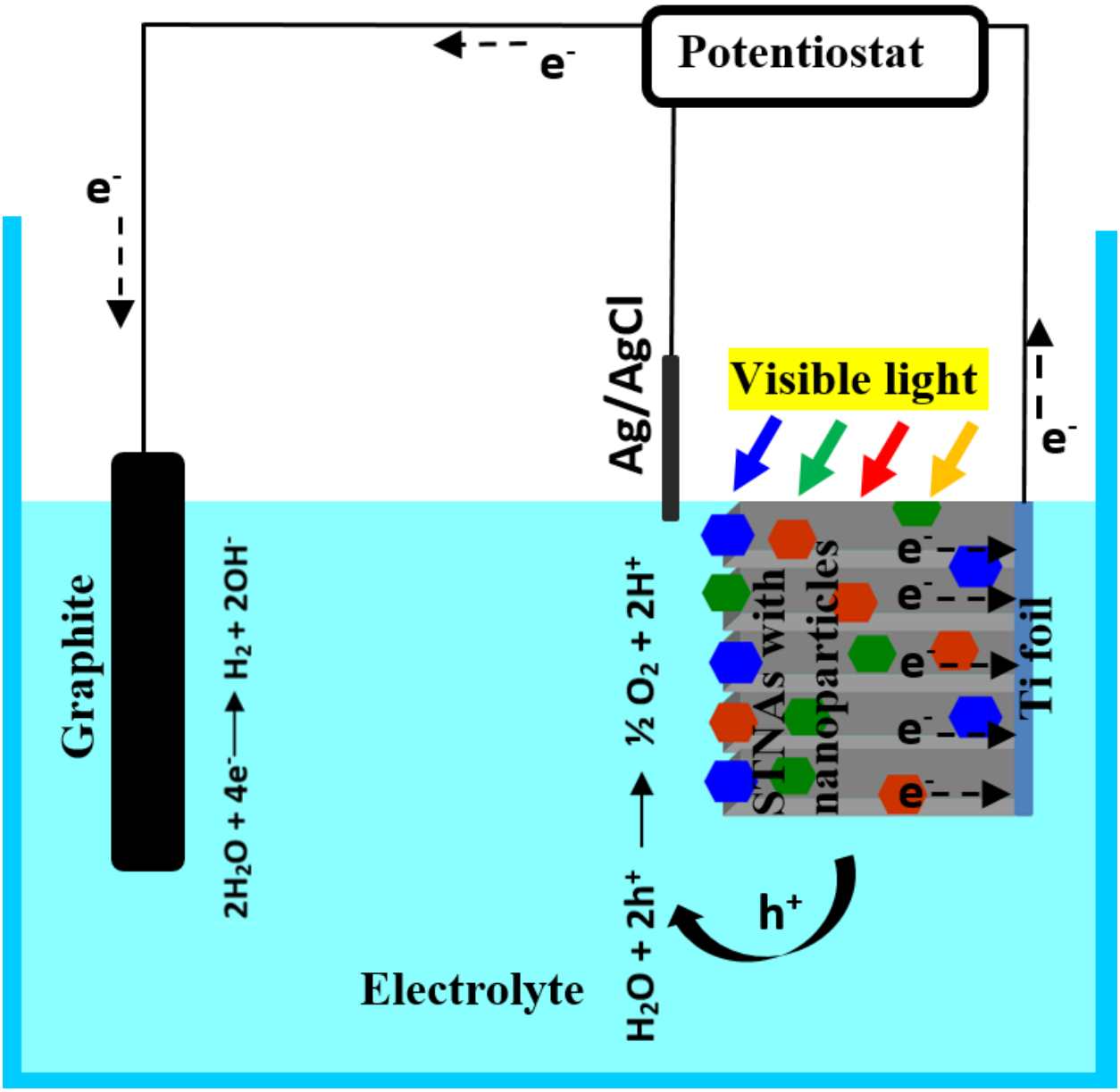

Fig S4. Schematic illustration of mechanism of the visible light photoelectrocatalysis process. The working electrode (i.e. STNAs with nanoparticles), due to the effect of Schottky barrier has electron-rich conduction band that transports electrons to the external circuit via the Ti foil, which serves as current collector. These electrons combine with protons at the counter-electrode electrolyte interface to generate hydrogen via the hydrogen evolution reaction.

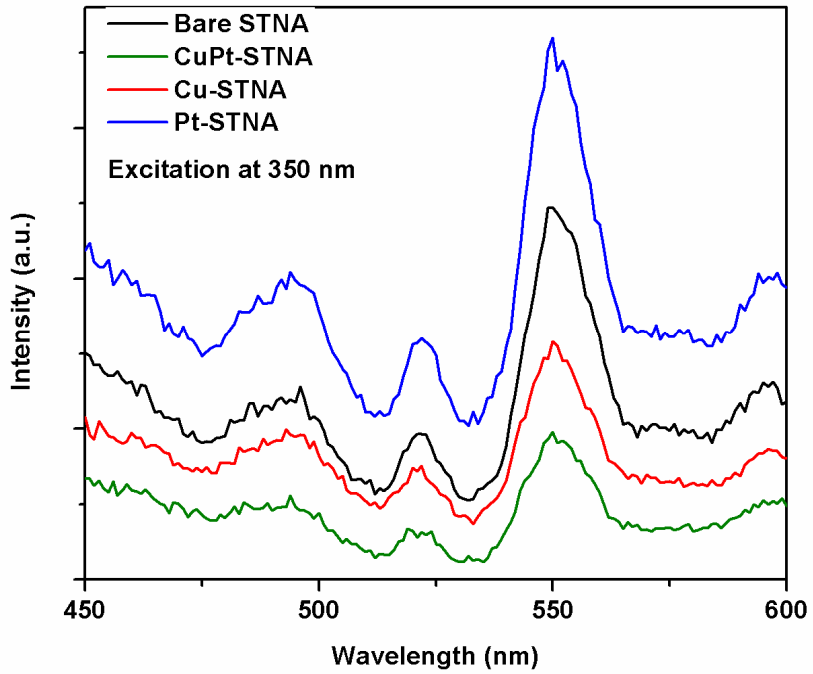
Bare STNA
CuPt-STNA
Cu-STNA
Pt-STNA
Excitation at 350 nm
Intensity (a.u.)
450
500
550
600
Wavelength (nm)

(a)

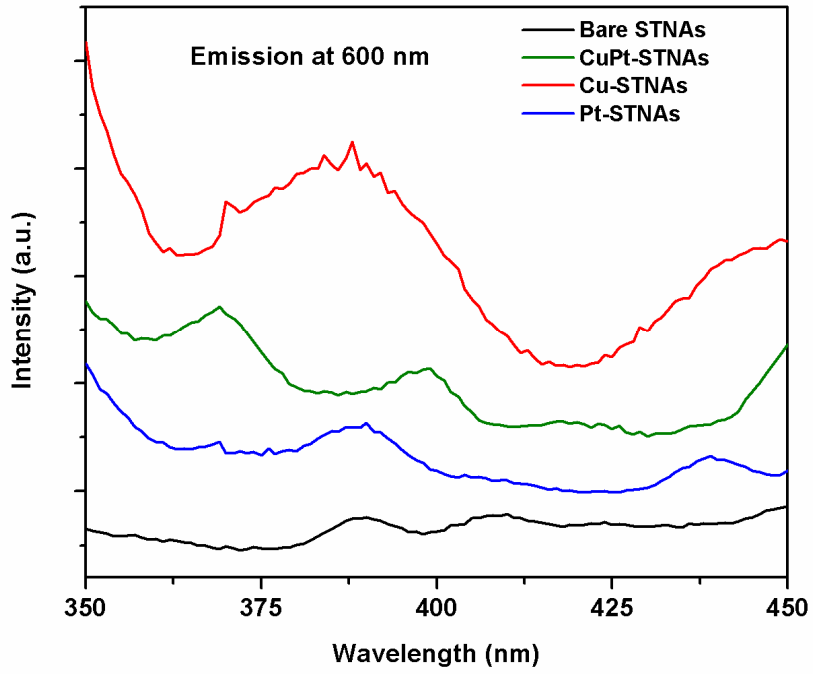
Emission at 600 nm
Bare STNAs
CuPt-STNAs
Cu-STNAs
Pt-STNAs
Intensity (a.u.)
350
375
400
425
450
Wavelength (nm)

(b)

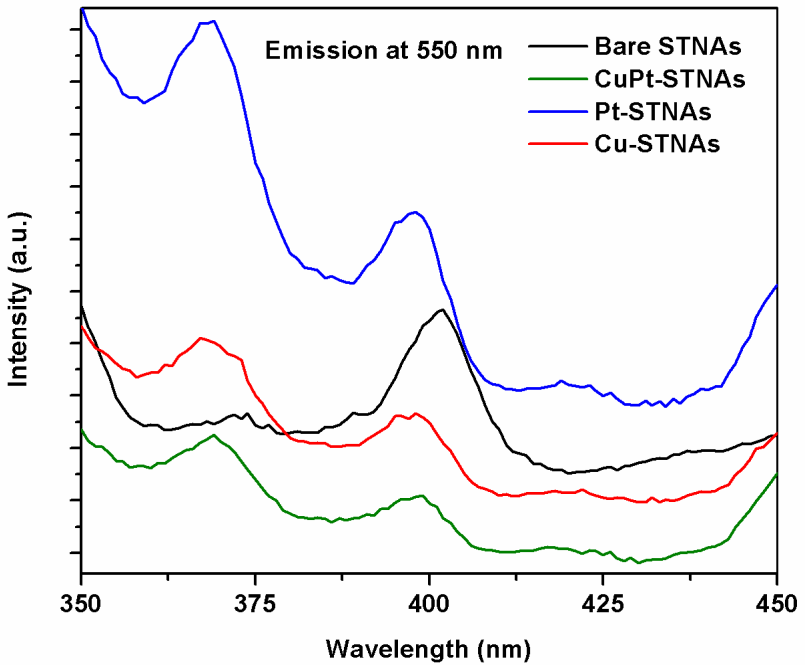

(c)

Fig. S5. PL spectra of the Cu, Pt and CuPt NPs incorporated STNAs and bare STNAs. (a) PL emission spectra at 350 nm excitation; (b) PL excitation spectra at 600 nm emission; and (c) PL excitation spectra at 550 nm emission;

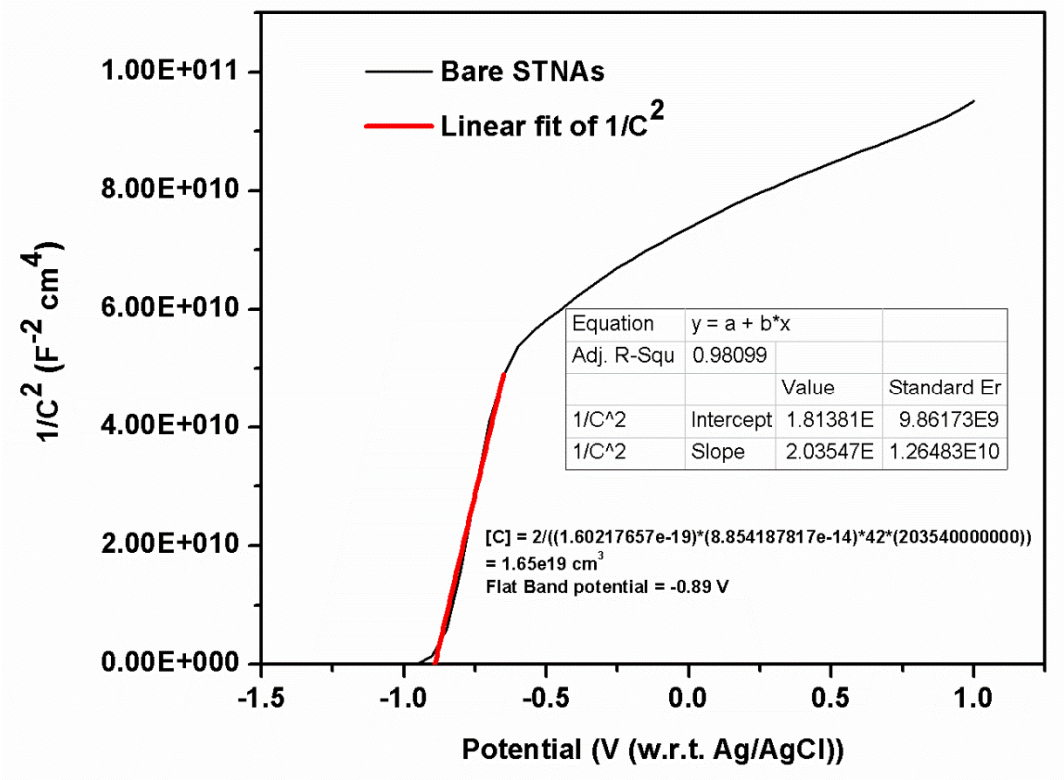
Bare STNAs
Linear fit of 1/C2
1.00E+011
8.00E+010
6.00E+010
4.00E+010
2.00E+010
0.00E+000
1/C2 (F-2 cm4)
-1.5
-1.0
-0.5
0.0
0.5
1.0
Potential (V (w.r.t. Ag/AgCl))
Equation y = a + b*x
Adj. R-Squ 0.98099
Value Standard Er
1/C^2 Intercept 1.81381E 9.86173E9
1/C^2 Slope 2.03547E 1.26483E10
[C] = 2/((1.60217657e-19)*(8.854187817e-14)*42*(203540000000))
= 1.65e19 cm3
Flat Band potential = -0.89 V

(a)

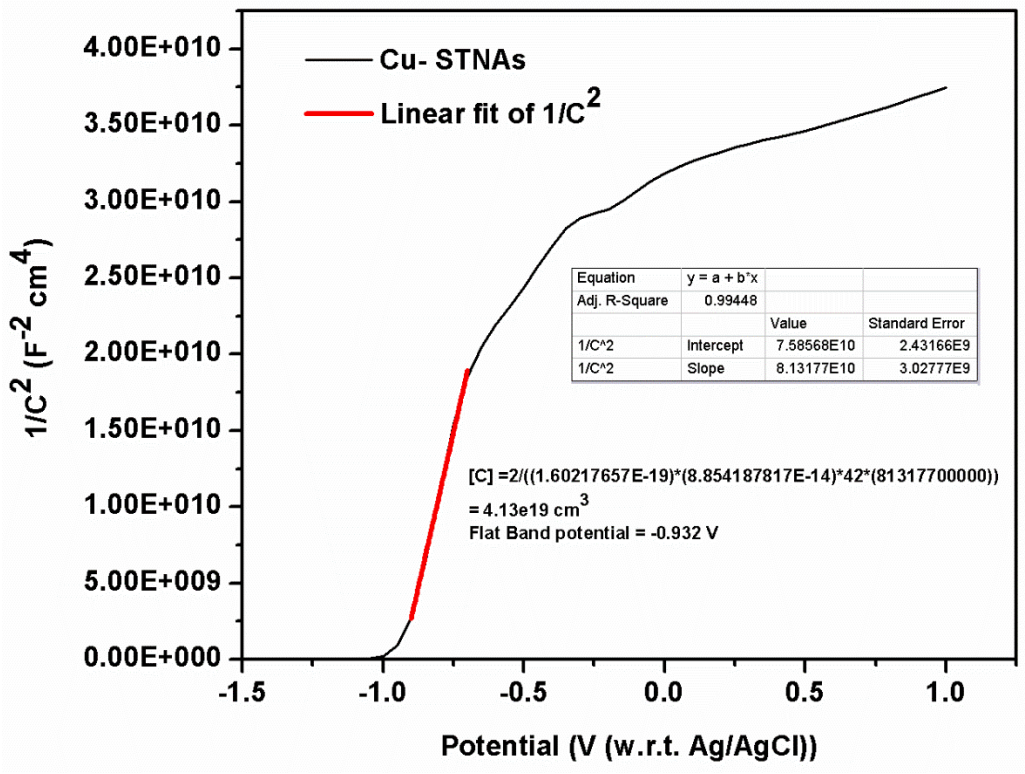
Cu- STNAs
Linear fit of 1/C2
4.00E+010
3.50E+010
3.00E+010
2.50E+010
2.00E+010
1.50E+010
1.00E+010
5.00E+009
0.00E+000
1/C2 (F-2 cm4)
-1.5
-1.0
-0.5
0.0
0.5
1.0
Potential (V (w.r.t. Ag/AgCl))
Equation y = a + b*x
Adj. R-Square 0.99448
Value Standard Error
1/C^2 Intercept 7.58568E10 2.43166E9
1/C^2 Slope 8.13177E10 3.02777E9
[C] =2/((1.60217657E-19)*(8.854187817E-14)*42*(81317700000))
= 4.13e19 cm3
Flat Band potential = -0.932 V

(b)

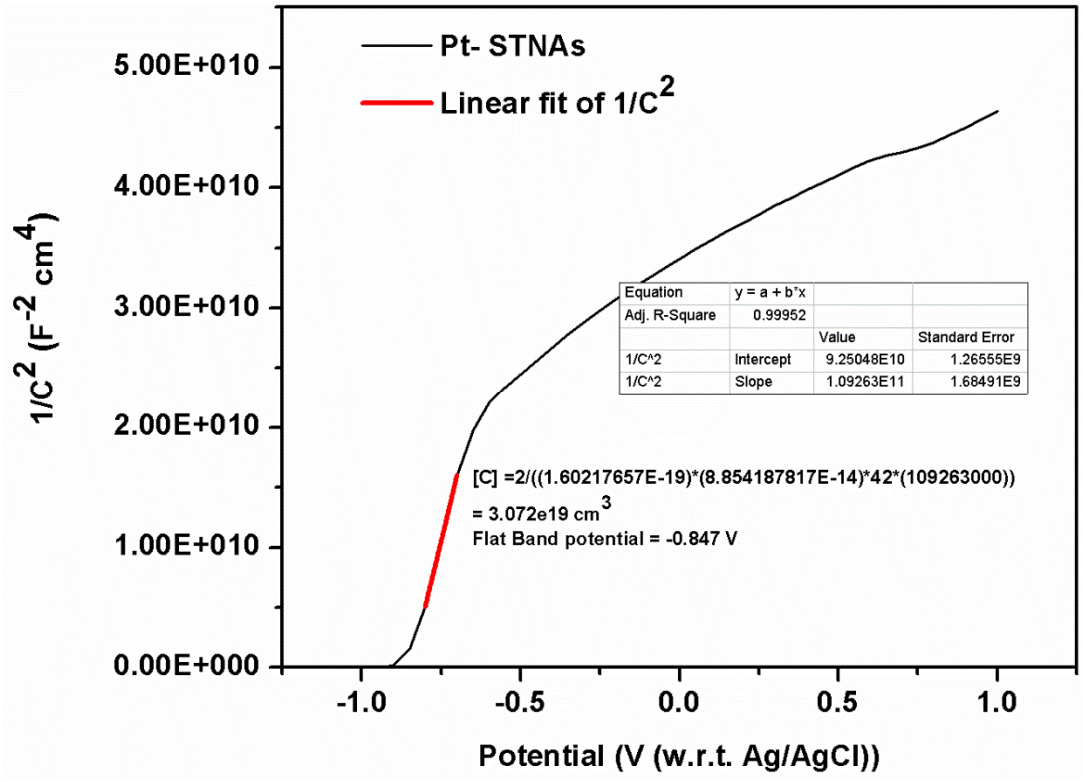
Pt- STNAs
Linear fit of 1/C2
1/C2 (F-2 cm4)
5.00E+010
4.00E+010
3.00E+010
2.00E+010
1.00E+010
0.00E+000
-1.0
-0.5
0.0
0.5
1.0
Potential (V (w.r.t. Ag/AgCl))
Equation y = a + b*x
Adj. R-Square 0.99952
Value Standard Error
1/C^2 Intercept 9.25048E10 1.26555E9
1/C^2 Slope 1.09263E11 1.68491E9
[C] =2/((1.60217657E-19)*(8.854187817E-14)*42*(109263000))
= 3.072e19 cm3
Flat Band potential = -0.847 V

(c)

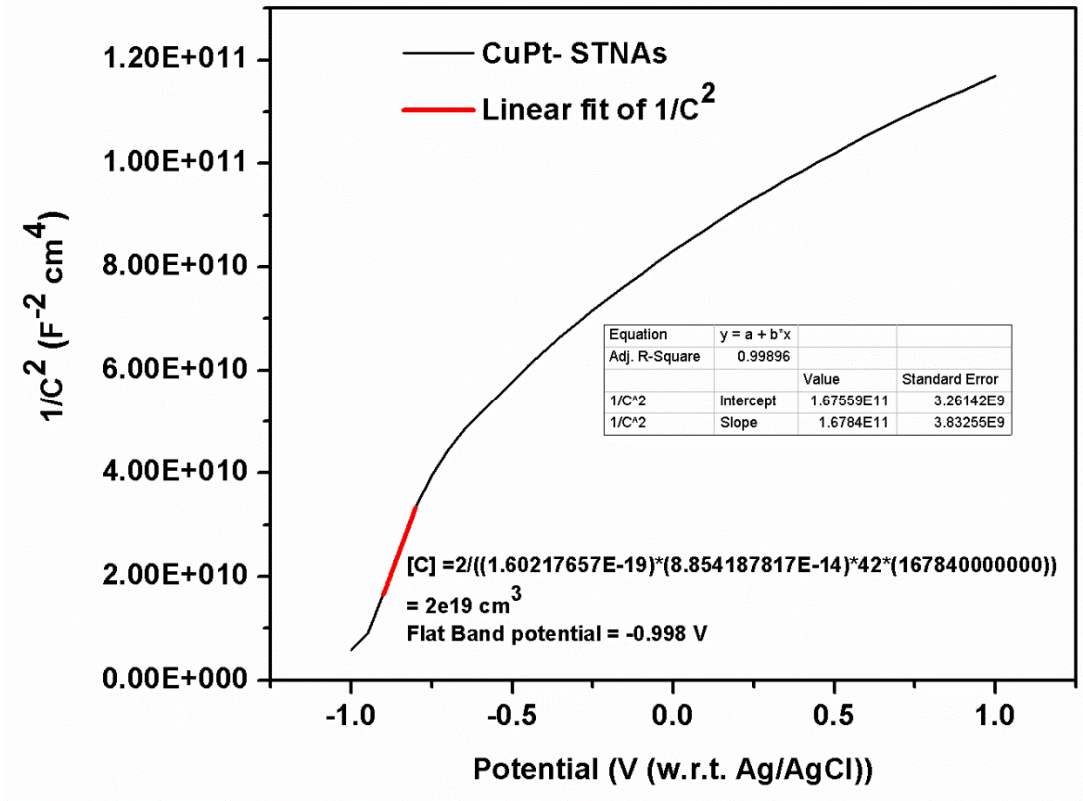
CuPt- STNAs
Linear fit of 1/C2
1/C2 (F-2 cm4)
1.20E+011
1.00E+011
8.00E+010
6.00E+010
4.00E+010
2.00E+010
0.00E+000
-1.0
-0.5
0.0
0.5
1.0
Potential (V (w.r.t. Ag/AgCl))
Equation y = a + b*x
Adj. R-Square 0.99896
Value Standard Error
1/C^2 Intercept 1.67559E11 3.26142E9
1/C^2 Slope 1.6784E11 3.83255E9
[C] =2/((1.60217657E-19)*(8.854187817E-14)*42*(167840000000))
= 2e19 cm3
Flat Band potential = -0.998 V

(d)

Fig. S6. Mott Schottky plots of (a) bare STNAs (b) Cu-STNAs (c) Pt-STNAs and (d) CuPt-STNAs were used to calculate the carrier concentration(s) and flat band potential(s); The carrier densities were obtained from figures (a-d) by considering the slope (***m***) of the straight line fits while the flat band potentials were obtained from the intercepts of the straight line fits. The values of carrier concentrations as determined are 4.13×10^{19} cm^{-3}, 3.07×10^{19} cm^{-3}, 2.00×10^{19} cm^{-3} and 1.65×10^{19} cm^{-3} for Cu-STNAs, Pt-STNAs, CuPT-STNAs and bare STNAs, respectively. Flat band potential values, as determined herein, are -0.932 V, -0.847 V, -0.998 V and -0.890 V w.r.t. Ag/AgCl for Cu-STNAs, Pt-STNAs, CuPt-STNAs and bare STNAs, respectively.

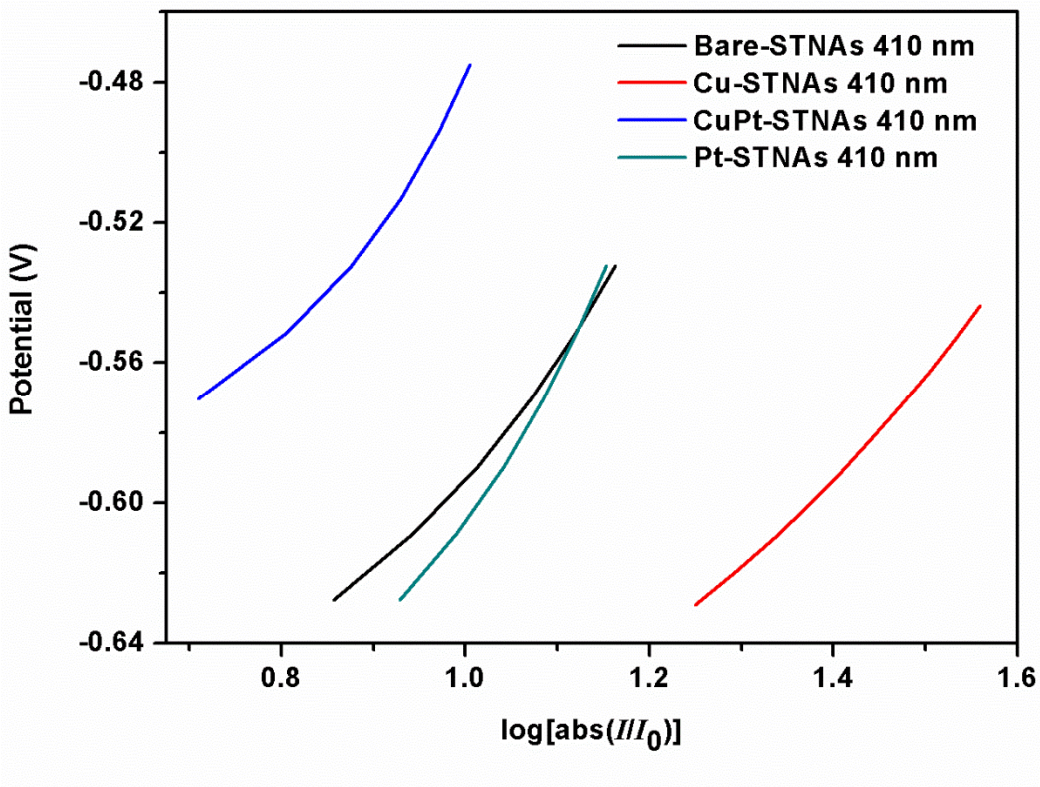

Fig. S7. Tafel curves for bare STNAs (a), Cu-STNAs (b), Pt-STNAs (c) and CuPt-STNAs (d). The plots show the straight lines fits used for determining Tafel slopes. Tafel slopes are 0.277, 0.423, 0.318, and 0.310 for Cu-STNAs, Pt-STNAs, CuPt-STNAs and bare STNAs, respectively. $\boldsymbol{I_0}$ is the exchange current density, $\boldsymbol{I}$ is the measure current, and V is potential versus Ag/AgCl

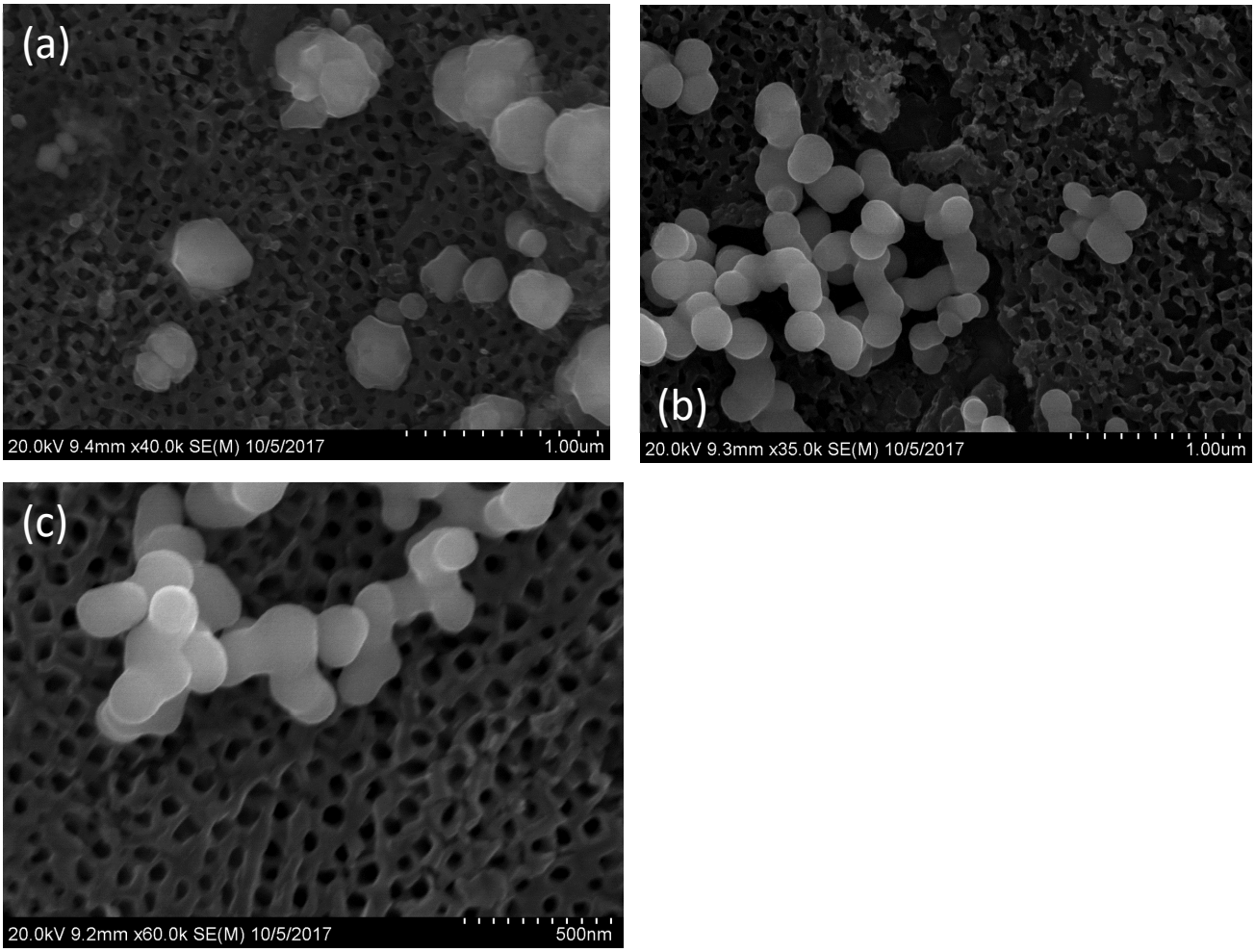

Fig. S8. FESEM images of Cu NPs (a), CuPt NPs (b) and Pt NPs (c) with increased metal nanoparticle loading showing large scale agglomeration of the nanoparticles. Due to agglomeration, our attempts to load more nanoparticles onto the nanotubes were not successful.